IVYSPRING INTERNATIONAL PUBLISHER

Theranostics

2026; 16(13): 7108-7123. doi: 10.7150/thno.129853

Research Paper

Porphyrin-lipid nanotheranostics for multimodal imaging of nodal disease in preclinical oral cancers

Michael S. Valic[1,2], Esmat Najjar[1,3,4], Mark Zheng[1], Jason L. Townson[1,3], Harley H. L. Chan[1,3], Sharon Tzelnick[1,3,4], Alessandra Ruaro[1,3,4], Abdullah El-Sayes[1], Michael Halim[1], Pamela Schimmer[1], Chris J. Zhang[1], Tina Ye[1], Wenlei Jiang[1], Juan Chen[1], Jonathan C. Irish[1,3,4]✉, Gang Zheng[1,2,5]✉

1. Princess Margaret Cancer Centre, University Health Network, Toronto, Canada.
2. Institute of Biomedical Engineering, Faculty of Applied Science and Engineering, University of Toronto, Toronto, Canada.
3. Guided Therapeutics Program, University Health Network, Toronto, Canada.
4. Department of Otolaryngology–Head and Neck Surgery, Temerty Faculty of Medicine, University of Toronto, Toronto, Canada.
5. Department of Medical Biophysics, Temerty Faculty of Medicine, University of Toronto, Toronto, Canada.

✉ Corresponding authors: Jonathan C. Irish, Princess Margaret Cancer Centre, University Health Network, 200 Elizabeth Street, 8NU-882, Toronto, ON M5G 2C4, Canada. E-mail: jonathan.irish@uhn.ca. Gang Zheng, Princess Margaret Cancer Centre, University Health Network, 101 College Street, PMCRT RM 5-354, Toronto, ON M5G 1L7, Canada. Phone: 416-581-7667; E-mail: gang.zheng@uhn.ca.

Received: 2025.12.12; Accepted: 2026.05.20; Published: 2026.05.29

Abstract

Rationale: Cervical lymph node metastases in oral cancer patients are a frequent occurrence and important prognostic factor. Anatomical and molecular imaging modalities can identify neck metastases with varying sensitivity and specificity but perform poorly in clinically negative neck nodes with microscopic disease. Herein we investigate the use of porphyrin-lipid nanotheranostics (PS) for multimodal detection of neck disease in preclinical models of oral cancer.

Methods: Xenograft models of tongue cancer were established in nude rats using MOC2 mouse oral squamous cells. PS nanoparticles were radiolabelled with positron-emitting Copper-64 (^{64}Cu-PS) and administered either IT (100 MBq ^{64}Cu, 0.5 mg) or IV (250–500 MBq ^{64}Cu/kg, 0.5–1.0 mg/kg). Uptake in the tumour and cervical lymph nodes was measured with serial PET/MR imaging and at endpoint with *in situ* fluorescence (FL) imaging. In the IV cohort, ^{64}Cu-PS uptake was compared to ^{18}F-FDG (46 MBq ^{18}F/kg) PET performed prior to nanoparticle injection. After imaging, neck nodes were harvested for pathological staging. Receiver operating characteristics were compared in the IV cohort between ^{18}F-FDG *vs* ^{64}Cu-PS PET imaging *vs* FL imaging.

Results: The tongue tumour model yielded micrometastases to 54% of neck nodes by 14 d post-implantation. Following IT injection, sentinel and metastatic lymph nodes were visible with ^{64}Cu-PS PET for 72 h. Following IV injection, ^{64}Cu-PS PET signal in the tumour and neck nodes was clearest at 24 h and significant differences in the pooled SUVs of benign *vs* metastatic nodes were obtained. On FL imaging, metastatic neck nodes had significantly higher fluorescent signal (S/B) compared to benign nodes. Overall, FL S/B_{mean} gave the best prediction of nodal disease with 75% SEN, 79% SPC, and 71% NPV. ^{64}Cu-PS PET (SUV_{max}: 77% SEN, 68% SPC, 68% NPV) performed slightly worse than FL imaging for identifying metastatic nodes but still better compared to ^{18}F-FDG PET (SUV_{max}: 81% SEN, 43% SPC, 59% NPV). Inflamed nodes were the commonest source of false positives for both ^{64}Cu-PS PET and FL imaging modalities.

Conclusions: Nanotheranostic ^{64}Cu-PS permitted more accurate multimodal detection of microscopic neck disease in preclinical oral cancer models and can offer valuable guidance for planning and performing neck dissections.

Keywords: nanoparticles; radiotracers; fluorescence; lymph node metastasis; oral cancers

Introduction

Oral cancers are a family of diseases originating primarily from the thin squamous cell lining on the insides of the lips, mouth, and throat (pharynx). An estimated 59,000 Americans will be newly diagnosed with oral cavity and oropharyngeal cancers in 2025 [1], the majority of whom will undergo surgical resection as their primary treatment. A key challenge in the management of these patients is the spread of disease to regional lymph nodes in the neck, estimated to affect up to 50% of patients with primaries located in the oral cavity [2–4]. Cancers in the oral tongue have the highest rate of cervical lymph

node metastasis at the time of surgery compared to all other sites in the mouth [1,5]. Unsurprisingly, neck disease is an important prognostic indicator for oral cancer patients, associated with higher rates of locoregional recurrence and poorer overall survival [6–8].

The detection of lymph node metastases in the neck presently relies on multimodal approaches combining manual palpation and anatomical imaging modalities like computed tomography (CT), magnetic resonance (MR), and ultrasound that use node morphology (e.g., volume) to identify suspicious nodes [9]. The performance of these image-based approaches for detecting neck disease varies widely across studies depending on the patient populations analysed (e.g., early *vs* advanced stage, primaries of oral cavity *vs* oropharynx) and morphological criteria employed [10,11]. Crucially, when studies compared the findings of neck examinations (palpation and imaging) to the pathological stage of dissected lymph nodes, between 10~30% of oral cancer patients with clinically negative (cN0) necks were revealed to have pathologically confirmed (pN+) lymph node metastases [12,13]. Therefore, uncertainties over the neck status of patients from clinical examination have resulted in current recommendations for routine elective neck dissections in patients with high-risk primaries [9].

Molecular imaging techniques using radiotracers and optical probes have been increasingly explored for providing complementary information to CT and MR imaging for guiding the management of the necks of oral cancer patients [14]. For example, the uptake of [^{18}F]Fluorodeoxyglucose (^{18}F-FDG) radiotracers in neck lymph nodes using positron emission tomographic (PET) imaging has demonstrated modest improvements for catching occult metastases in cN0 necks [11,15]; yet ^{18}F-FDG PET, like all the other imaging modalities, is insufficiently reliable for detecting microscopic neck disease to eliminate the need for elective neck dissections in high-risk patients [16–18]. In intraoperative settings, real-time fluorescence (FL) imaging with optical probes targeting the tumour biology of oral cancers has shown promise in clinical studies for clearing surgical margins [19,20], and mapping metastatic and sentinel lymph nodes in the neck [21,22]. Ultimately, there is still a need for imaging agents that can provide more accurate staging of neck disease preoperatively, guide lymph node dissections intraoperatively, and ideally both.

Our group has previously reported the development of Porphysomes (PS), multifunctional porphyrin-lipid nanotheranostics for fluorescence-guided surgery and photodynamic ablation of oral cancers [23–25]. In a rabbit VX-2 buccal tumour model, Muhanna *et al.* demonstrated with FL imaging a > 2-fold enhancement of PS fluorescence in suspicious neck nodes, which was used to guide lymph node biopsies and neck dissections [23]. The porphyrin building blocks of PS also serve as chelators for transition radiometals such as positron-emitting Copper-64 (^{64}Cu) [26,27]. Using ^{64}Cu-radiolabelled PS, the authors showed that uptake of ^{64}Cu-PS radiotracers in VX-2 oral tumours provided clear tumour delineation and detailed mapping of sentinel and metastatic lymph nodes in the rabbit neck on PET [23]. Altogether these previous data suggest that multimodal ^{64}Cu PET and FL imaging with PS may fill a major gap in the clinical management of occult neck metastases in oral cancer patients.

The present study is a comprehensive investigation of ^{64}Cu-labelled PS nanotheranostics for multimodal staging of metastatic disease in the cervical lymph nodes of preclinical models of oral cancer. A xenograft model of squamous cell carcinoma (SCC) was established in the tongues of nude rats, giving rise to reproducible micrometastases in the neck lymph nodes (Fig. 1). ^{64}Cu-PS were administered either intratumourally (IT) or intravenously (IV), and their uptake in tongue tumours and cervical nodes imaged with serial PET/MR and *in situ* FL. After imaging, all the neck nodes were dissected and submitted for blinded pathological staging. Receiver operating characteristics (ROC) testing the accuracy for identifying pN0 *vs* pN+ staged lymph nodes were calculated for both ^{64}Cu-PS PET and FL imaging modalities and compared to tests using nodal morphology (from MRI) or ^{18}F-FDG uptake. Altogether, these studies aim to answer whether ^{64}Cu-PS nanotheranostics permit more accurate multimodal detection of microscopic neck disease in preclinical oral cancer models *vs* existing clinical imaging modalities.

Materials and Methods

Materials and reagents

PS are PEGylated pyro-lipid nanoparticles [28] consisting of 55 mol% pyro-lipid (University Health Network, Toronto, Canada), 40 mol% cholesterol (CH-0355; CordenPharma, Liestal, Switzerland), and 5 mol% N-(carbonyl-methoxypolyethyleneglycol-2000)-1,2-distearoyl-sn-glycero-3-phosphoethanolamine (LP-R4-039; CordenPharma). ^{64}Cu chloride ([^{64}Cu]$CuCl_2$) was purchased from the University of Wisconsin Institutes for Medical Research Cyclotron Labs (Madison, USA). Protocol for radiolabelling

^{64}Cu-PS has been previously described [27]: the radiochemical purity of ^{64}Cu-PS used for animal experiments was 96.6 ± 1.1% from instant thin layer chromatography and the A_s was 503 ± 98 MBq ^{64}Cu/mg pyro-lipid. Physicochemical properties of PS and ^{64}Cu-PS are provided in Fig. S1. Chelation stability of ^{64}Cu-PS has been previously confirmed under physiological conditions [26,27]. ^{18}F-FDG was purchased from Isologic Innovative Radiopharmaceuticals (Toronto, Canada) and was used as supplied.

Development of tongue tumour xenograft model with neck metastasis

Mouse oral squamous cell carcinoma (MOC2) cells (EWL00w-FP; Kerafast, Shirley, USA) derived from a chemokine receptor CXCR3-deficient C57BL/6 mouse [29] were cultured per the supplier's protocol. Authentication testing of MOC2 cells was performed using short tandem repeat profiling and Mycoplasma testing completed by polymerase chain reaction. Cells were used for animal experiments after ≤ 10 passages. Female athymic nude rats (Hsd:RH-*Foxn1*^{rnu}) were purchased from Invotiv (Livermore, USA). On the day of tumour implantation, animals weighed 221 ± 35 g. Under inhaled anaesthesia, a single cell suspension of 100,000 MOC2 cells in 0.15 mL phosphate buffered saline was injected into the body of the tongue using a 29 Ga needle. Post procedure, animals were housed in pairs, provided an irradiated alfalfa-free diet (TD.94045; Inotiv) and water *ad libitum*. Animal weight and clinical condition were monitored daily. Summary of experimental details for each animal is provided in Table S1.

PET/MR imaging in tongue tumour model

PET/MR imaging was performed using a 1T PET/MR small animal scanner (nanoScan; Mediso, Budapest, Hungary). For intratumoural lymphatic mapping experiments, ^{64}Cu-PS (80–120 MBq ^{64}Cu, 0.5 mg pyro-lipid, IT) were administered into the tongue tumour in a 0.05–0.1 mL volume using a 31 Ga hypodermic needle. PET/MR imaging was performed at timepoints: 1 h, 3 h, 6 h, 12 h, 24 h, 48 h, and 72 h post-IT injection. PET acquisition times ranged from 10–25 min and T1 3D material maps were collected for MRI-based attenuation correction using parameters: 256 x 182 matrix, 0.35 x 0.35 x 0.60 mm^3 voxel size, 18.98 ms repetition time, 2.9 ms echo time, 15° flip angle.

For comparison experiments between systemically injected PET radiotracers, ^{18}F-FDG was injected and imaged 24 h prior to experiments involving ^{64}Cu-PS. Rats were fasted overnight and blood glucose measured ~4.9 mmol/L before injection. ^{18}F-FDG (46 MBq ^{18}F/kg, IV) was administered via the tail vein and PET/MR imaging performed after ~45 min of uptake. PET acquisition time was 10 min using the same imaging parameters described above. The following day, ^{64}Cu-PS (250–500 MBq ^{64}Cu/kg, 0.5–1.0 mg/kg pyro-lipid, IV) were administered via tail vein and PET/MR imaging repeated as described above at 3 h and 24 h post-IV injection using a 15–20 min PET acquisition time.

All PET images were reconstructed using parameters: 400-600 keV energy window, 105 x 105 x 237 matrix, 0.4 mm^3 voxel size. Image analysis was performed in Inveon Research Workplace (Ver. 4.2.0.15; Siemens Medical Solutions, Malvern, USA). Volumes of interest (VOIs) were manually created by trained readers for the tongue tumour, benign tongue, and any cervical lymph nodes visualised with PET and/or MR. The mean and maximum standardised uptake values (SUV) were generated for the tumour and lymph node VOIs for quantitative analysis and statistical testing. Lymph nodes that were nonvisible on PET imaging were given SUV values equivalent to background uptake in benign tongue. MIPs of PET/MR images were exported with arbitrary scales for PET intensity.

In situ fluorescence imaging

Animals were euthanised and the cervical lymph nodes exposed. A white light image of the neck was captured. Animals were positioned in an IVIS Spectrum *In Vivo* Imaging System (PerkinElmer; Shelton, USA) for FL imaging using filter setting: 675 nm Ex, 720+ nm Em, 1–5 s exposure, 1.5 cm (height) focus. The FL images were opened in Live Image software (Ver. 5.4.2.18425; PerkinElmer) and regions of interest (ROIs) created over the nodes and mandibular gland. The mean and maximum fluorescence radiant efficiency (units = [p/s/cm^2/sr]/[μW/cm^2]) was extracted from each ROI. The relative fluorescence in the lymph nodes was calculated as signal-to-background (S/B) ratio using the 'background' fluorescence in the mandibular gland. The mean and maximum S/B ratios were calculated in the lymph node ROIs for quantitative analysis and statistical testing.

Lymph node histopathology

The tongue tumours and lymph nodes were harvested for histological processing after imaging. Tissue dyes were used for marking the anatomical positioning of the neck nodes prior to submission. For routine processing, tissues were formalin fixed, paraffin embedded, and cut sections were stained for H&E and cytoplasmic cytokeratin (CK) (NBP2-29429; Novus Biologicals, Toronto, Canada) per laboratory

standard procedures. Two or three levels, separated by ~0.25 mm, were cut from each paraffin block and slides scanned with 20x magnification. For ^{64}Cu tissue autoradiography, the harvested tissues were embedded in O.C.T. compound (SGN4585; Fisher Healthcare, Houston, USA) and flash frozen in liquid nitrogen before cutting on a cryostat with 30 µm slice thickness. The autoradiography slides were exposed against a high-resolution storage phosphor screen (7001487; PerkinElmer) for ~24 h before imaging at 600 DPI (~42 µm/pixel) resolution using a phosphor imaging system (Cyclone Plus; PerkinElmer). Additional slides were cut from frozen blocks for H&E, CK, and CD68/SR-D1 (NB100-683; Novus Biologicals) staining and fluorescence microscopy using 4′,6-diamidino-2-phenylindole (DAPI) (D1306; Thermo Fisher Scientific) and FITC-tagged CK (NBP2-33200F; Novus Biologicals). Fluorescence scans (Axioscan 7; Carl Zeiss Microscopy, Jena, Germany) were acquired with 20x resolution using DAPI and Cy5 filters (Cy5 overlaps with the fluorescence wavelength of pyro-lipid).

Pathological staging of lymph nodes was performed by clinical readers blinded to the imaging data using the AJCC TNM cancer staging system [30,31]: nodes with no detectable CK$^+$ cellular staining or having isolated tumour cells defined as CK$^+$ metastatic foci ≤ 0.2 mm and lacking clustering pattern were considered node-negative (pN0); nodes with micrometastasis defined as CK$^+$ metastatic foci > 0.2 mm and ≤ 2.0 mm (or ~200 CK$^+$ cell clusters) were considered node-positive (pN+). Slide scans were viewed and measured in QuPath (Ver. 0.5.1; The University of Edinburgh, Edinburgh, UK). No nodes in this study (N=114) presented with tumour deposits > 2.0 mm (macrometastasis). Extracapsular disease spread from lymph nodes was extremely rare (N=2).

Receiver operating characteristics analysis

ROC curves were created by plotting true positive rate *vs* false positive rate. 95% C.I. for area under the ROC curve (AUC) was calculated using nonparametric methods. The optimal cutoff values of the diagnostic tests reported in the text and figures used the Youden index; results with other cutoff value methods are reported in Table S10. Equations for calculating diagnostic test results are provided in the Supplemental Data.

Statistical analysis

Statistical testing was performed using Prism (Ver. 10.3.1 (464); GraphPad Software, Boston, USA) or MATLAB (Ver. R2023b Update 4; The MathWorks, Natick, USA). Post-hoc power analyses were performed using G*Power software (Ver. 3.1.9.6; Heinrich Heine Universität Düsseldorf, Düsseldorf, Germany) and are provided in the Supplemental Data. Mean ± 1 S.D. reported in text. Box and whisker plots use Tukey's method and "+" to denote sample means. Multiplicity adjusted P values and $\alpha = 0.05$ were used throughout. P values: not significant (ns) > 0.05, * ≤ 0.05, ** ≤ 0.01, *** ≤ 0.001.

Results

Development of an oral cancer neck metastasis model

By 10–14 d post-implantation of murine MOC2 SCC cells, the tongue tumours had reached 171 ± 84 mm^3 from MR imaging and rat body weights had decreased ~5%. At the time of experimentation, 54% (61/114) of all the cervical lymph nodes harvested for histopathology demonstrated evidence of microscopic tumour cell clusters measuring > 0.2 mm from CK immunohistochemical staining (Fig. 1C). An additional 43 nodes had microscopic evidence of isolated CK$^+$ tumour cells on at least one slide level; these nodes were staged pN0 in this study for consistency with clinical standards regarding isolated tumour cells [30,31]. Neck nodes from anatomical level 1 (i.e., superficial cervical nodes) located closest to the tongue tumour exhibited a 66% (50/76) prevalence rate for pN+ staging whereas the more distantly located central cervical nodes in level 2 had a pN+ prevalence rate of 32% (12/38). There were no incidences of lymph node macrometastasis > 2 mm, nor any skip nodal metastases to the central (level 2) cervical nodes detected in this model. Overall, the pattern of cervical node metastases in our preclinical model is similar to the reported distribution pattern of neck metastases in clinical patients with primaries in the oral cavity [4,5].

The volumes of cervical lymph nodes were also measured with MR imaging and analysed retrospectively once the pathological stage was known. In Fig. 1D, no meaningful differences in the volumes of pN0 (15.3 ± 8.2 mm^3) *vs* pN+ (16.5 ± 12.6 mm^3) staged nodes were observed. A diagnostic test using lymph node volume (Fig. 1E) to identify nodal disease performed no better than a random classifier (i.e., coin flip) in this preclinical neck metastasis model.

Sentinel and metastatic lymph node mapping with intratumoural ^{64}Cu-PS injection was nondiagnostic

Lymphatic mapping with ^{64}Cu-PS was performed in the tongue tumour model using serial PET/MR imaging to track the drainage of nanoparticles from the intratumoural injection site to

the cervical lymph nodes (Fig. 2A). Lymph nodes were clearly visible in the neck from PET imaging starting as early as 1 h post-IT injection and reached a peak contrast by 12~24 h. Minimal cervical lymphatic drainage of ^{64}Cu-PS nanotheranostics was observed after injection into the tongues of healthy rats (Fig. 2B), suggesting that lymphatic flow rate or volume draining from the tongue is enhanced by the presence of the tumour.

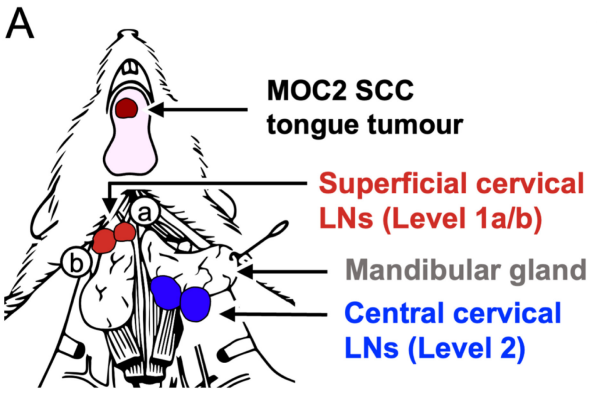

C

Pathological staging summary				
Lymph nodes		**N**	**pN0**	**pN+**
L1	a	38	18%	82%
	b	38	50%	50%
	both	76	24%	66%
L2		38	68%	32%
All		114	46%	54%

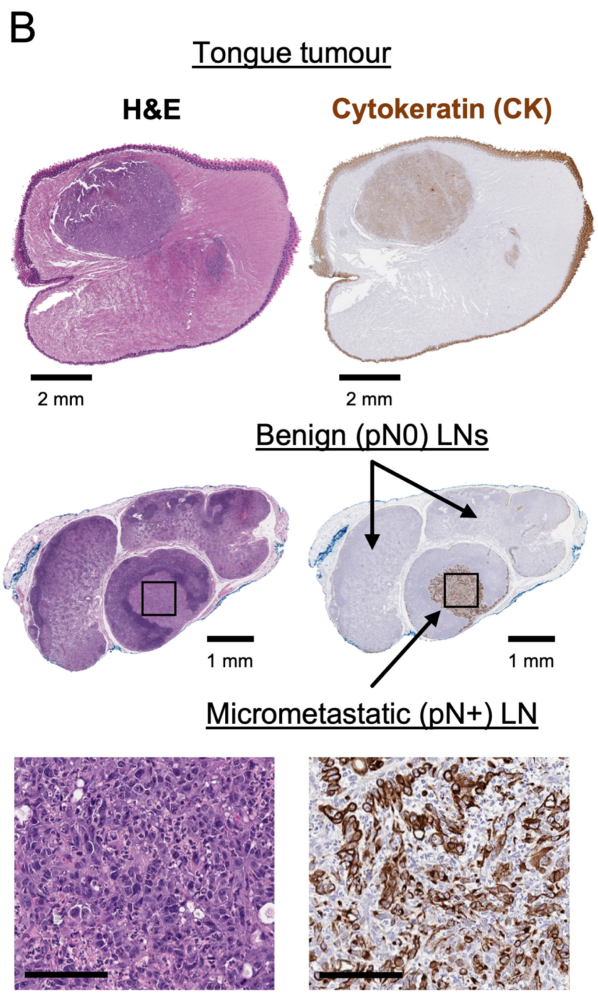

D

Lymph node volume measurements from MRI				
Lymph nodes		**pN0**	**pN+**	**pN0 *vs* pN+**
L1	a	14.3 ± 7.9	19.4 ± 17.4	ns
	b	18.6 ± 9.3	15.8 ± 4.9	ns
	both	16.9 ± 8.9	17.9 ± 13.8	ns
L2		12.8 ± 6.6	11.8 ± 5.5	ns
All		15.3 ± 8.2	16.5 ± 12.6	ns

Mean ± 1 S.D. Units mm^3.

E

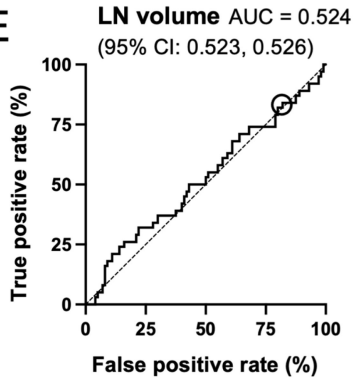

Cut off	LN vol. ≥ 10.1 mm^3
TP	41
FP	28
FN	11
TN	10
SEN	79%
SPC	26%
ACC	57%
NPV	48%
DOR	1.3

Figure 1. Characterisation of the preclinical model of oral cancer with neck metastases. (A) Head and neck anatomy of rodent model with a MOC2 tongue tumour. (B) Histopathology of tongue tumour and neck nodes containing a CK$^+$ micrometastasis. Scale bar for histology insets 100 µm. (C) Summary of anatomical distribution and pathological staging of all neck nodes included in study. (D) Summary of lymph node volumes from MR imaging according to anatomical level and pathological staging. Mean ± 1 S.D. Units mm^3. Statistics compare pN0 *vs* pN+ staged nodal volumes using multiple comparison t-tests with Tukey correction. (E) ROC curve and diagnostic performance of test predicting pN+ staged nodes using nodal volume from MR imaging. ROC AUC and 95% C.I.s listed in brackets.

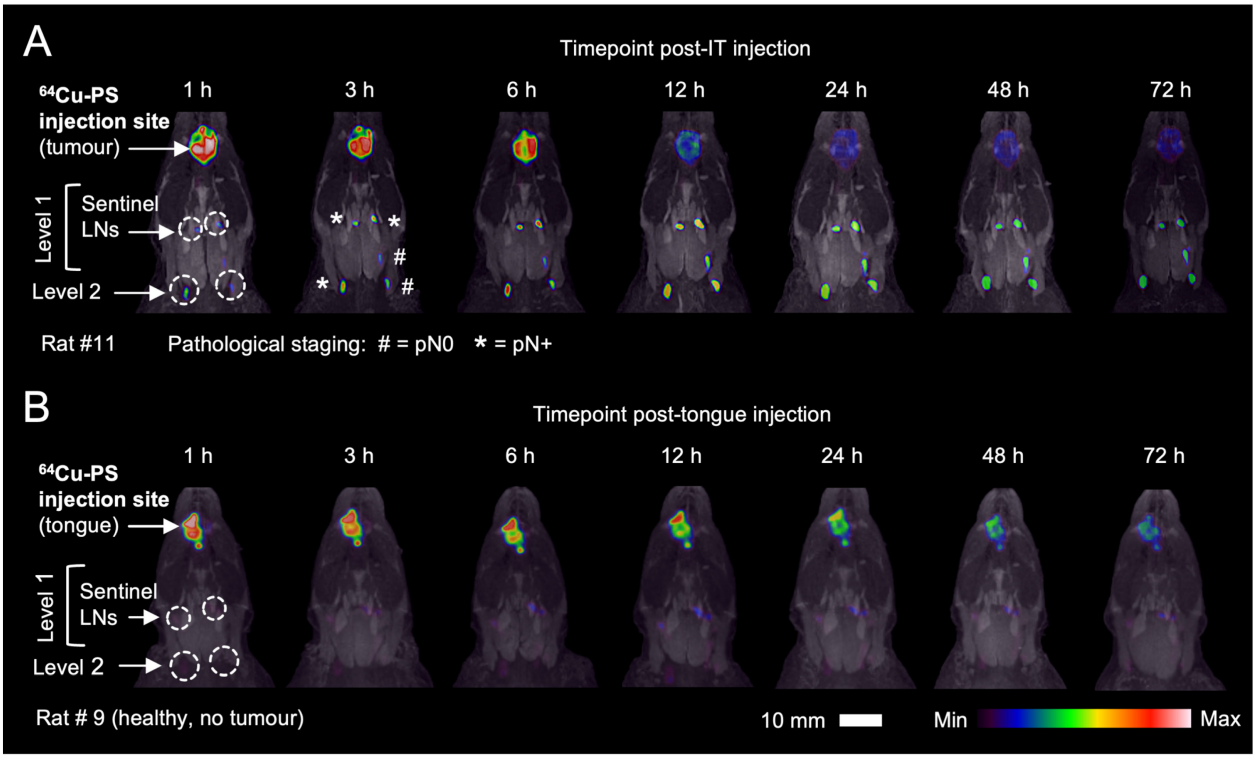

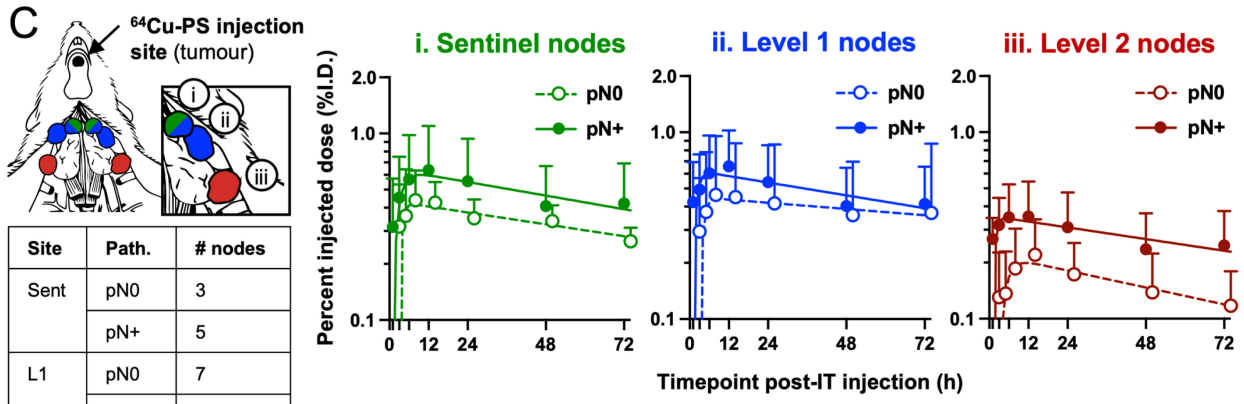

Site	Path.	# nodes
Sent	pN0	3
	pN+	5
L1	pN0	7
	pN+	8
L2	pN0	5
	pN+	3

Figure 2. Lymphatic mapping in tongue tumour model with IT injection of ^{64}Cu-PS. (A) Representative MIPs from serial ^{64}Cu-PS PET/MR imaging post-IT injection (80–120 MBq ^{64}Cu, 0.5 mg pyro-lipid). Pathological staging of nodes indicated on 3 h image. ^{64}Cu PET signal intensity arbitrarily scaled to the 1 h timepoint. (B) Healthy rats (i.e., without tongue tumours) administered ^{64}Cu-PS into the tongue and serially imaged. ^{64}Cu PET signal intensity scaling as in (A). (C) Image-based analysis of ^{64}Cu-PS pharmacokinetics in the sentinel lymph nodes, and in nodes from levels 1 and 2 by pathological status. Number of nodes listed in table for panel (C). Units %I.D. Means + 1 S.D. Trend lines are empirical fitting through mean value at each timepoint.

Analysing the pharmacokinetics of ^{64}Cu-PS in the tumour-draining lymph nodes with respect to pathological staging (Fig. 2C) revealed that pN+ staged nodes exhibited both a greater absolute accumulation of nanoparticle and a longer retention time (i.e., larger AUC) post-IT injection. However, the kinetic differences between pN0 and pN+ neck nodes were not statistically significant at any level analysed (see Table S3). Considerable differences were noted in the clearance rates of ^{64}Cu-PS from the IT injection site ($t_{1/2}$ ~19.8 h) *vs* from the sentinel nodes ($t_{1/2}$ ~89.7 h), suggesting potentially distinct biological mechanisms of nanoparticle retention in tumours and draining lymph nodes. In summary, ^{64}Cu-PS PET signal in tumour-draining neck nodes following IT injection may be helpful for preoperative planning of neck dissections but does not provide reliable diagnostic information on the pathological staging of occult lymph nodes from oral cancers.

^{64}Cu-PS passively accumulate in the tongue tumour following IV injection

In the context of oral cancers, IV injection is a more useful route for administering imaging agents owing to the highly complex patterns of lymphatic drainage in the neck (and correspondingly complex pathways of possible lymphatic metastasis from oral cavity tumours) [32,33]. The kinetics of ^{64}Cu-PS uptake in the preclinical oral cancer model was first established using serial PET/MR imaging at 3 h and 24 h post-IV injection (Fig. 3). PET imaging using ^{18}F-FDG (^{18}F physical $t_{1/2}$ 109 min) was also performed in the same rats 24 h prior to ^{64}Cu-PS experiments to compare differences in uptake between the canonical glucose metabolism-based PET radiotracer and nontargeted PS nanoparticles.

After IV injection, ^{64}Cu-PS were predominantly in blood circulation at the 3 h imaging timepoint and significant nonspecific PET signal was observed from healthy tissues in the neck and mouth (Fig. 3A). By 24 h, far better PET image contrast was obtained in the tongue tumour and the cervical lymph nodes, similar to the contrast seen with ^{18}F-FDG PET after 45 min uptake. From 3 h to 24 h post-IV injection, the SUV_{mean} of ^{64}Cu-PS nanoparticles in the tongue tumour significantly increased from 2.41 ± 0.73 to 4.39 ± 1.80 (P value < 0.001, Power = 0.83, see Fig. S2). In healthy rats without tongue tumours, low and nonspecific uptake of ^{64}Cu-PS was observed in the cervical nodes (Fig. 3B), similar to the pattern observed in the necks of healthy rats after local injection of nanoparticles into the tongue (see Fig. 2B).

The localisation of ^{64}Cu-PS in CK$^+$ squamous cell tumours was visualised in tongue histology using tissue autoradiography and fluorescence microscopy (Fig. 3C). A high correspondence between the ^{64}Cu autoradiography intensity and the fluorescence signal from the pyro-lipid building blocks of PS was observed, suggesting excellent chelation stability of ^{64}Cu-PS *in vivo*. Nonuniform distribution of ^{64}Cu-PS in the tumour cross-section was also noted, favouring the tumour periphery where it is presumed that blood vessels are still well perfused and the draining lymph vessels are functionally patent.

^{64}Cu-PS PET detects metastatic lymph nodes with greater accuracy than ^{18}F-FDG PET

As observed in Fig. 3A, the PET imaging contrast from ^{64}Cu-PS in the tongue tumour and cervical lymph nodes was optimal at 24 h post-IV injection (Fig. 4A). Nearly all the neck nodes (50/60, or 83%) harvested for histopathology were successfully visualised with ^{64}Cu-PS PET imaging at 24 h, two more than were visualised with ^{18}F-FDG PET. The neck nodes missed by ^{64}Cu-PS PET imaging were exclusively from anatomical level 2 and only 2/10 (20%) missed nodes contained pathologically confirmed micrometastases.

Pooling together the uptake in lymph nodes from all anatomical levels of the neck, there was significantly greater uptake in pN+ *vs* pN0 staged nodes measured using both SUV_{mean} and SUV_{max} (Fig. 4B). Analysing neck nodes from anatomical level 1 only, the difference in SUV_{max} between pN0 and pN+ nodes was also statistically significant with sufficient power (Fig. 4C). In level 2, pN+ staged nodes had slightly higher uptake than pN0 nodes but this difference was not significant for either SUV_{mean} or SUV_{max} (Fig. 4D). From the uptake data of ^{18}F-FDG PET imaging in the same rats, we observed no significant difference in SUV between pN0 and pN+ staged nodes and in fact greater uptake of ^{18}F-FDG on average in the pN0 nodes (see Fig. S3).

From the ROC curves for ^{64}Cu-PS PET imaging in Fig. 4E, a greater AUC was obtained using SUV_{max} and completely overlapped the ROC curve for SUV_{mean}. Using an optimal cutoff value of $SUV_{max} \geq 1.74$ provided 77% SEN, 68% SPC, 73% ACC, and 68% NPV for diagnosing pN+ staged nodes. False positive nodes were mostly from anatomical level 1 (63%), while 5/8 (63%) false negative nodes from ^{64}Cu-PS PET were from level 2. In contrast to ^{64}Cu-PS, using the SUV_{max} from ^{18}F-FDG PET imaging achieved only 81% SEN, 43% SPC, 67% ACC, and 59% NPV for diagnosing pN+ staged nodes (see Fig. S3).

In situ ^{64}Cu-PS FL imaging outperformed PET imaging for detection of neck disease

After PET imaging at 24 h post-IV injection, the rats were sacrificed and the neck nodes exposed for *in situ* FL imaging of ^{64}Cu-PS (Fig. 5). Note that the PS fluorescence signal (emission peak at 671 nm) was not strong enough to visualise through the skin. In Fig. 5A, the lymph nodes were clearly visualised amidst the complex anatomy of the neck using PS fluorescence: 86% (67/78) of all the cervical lymph nodes harvested for histopathology were more fluorescent than the mandibular gland (selected as background for the S/B calculations).

Pooling together the S/B ratios of nodes from all anatomical levels in the neck, significantly greater relative PS fluorescence was detected in pN+ *vs* pN0 staged nodes whether using S/B_{mean} or S/B_{max} ratios (Fig. 5B). Analysing the nodes from level 1 only, we observed that the difference in PS fluorescence between pN0 and pN+ nodes was still statistically significant and sufficiently powered for both ratios (Fig. 5C). However, pN+ staged nodes from level 2 only were just slightly more fluorescent than pN0 nodes and from background fluorescence in the

mandibular gland (Fig. 5D). Objectively, lymph nodes from level 2 were less fluorescent on average than those from level 1 receiving lymphatic drainage directly from the tongue tumour; this observation matches the data trend from ^{64}Cu-PS PET imaging showing higher uptake in level 1 *vs* level 2 nodes at 24 h post-IV injection.

From the ROC curves for *in situ* ^{64}Cu-PS FL imaging in Fig. 5E, the greatest AUC was obtained using the S/B_{mean} ratio for diagnostic testing. The curve for S/B_{mean} also overlapped the ROC curves for S/B_{max} and from ^{64}Cu-PS PET imaging in Fig. 4E, suggesting that ^{64}Cu-PS FL imaging can be used as a standalone modality for diagnosing lymph node metastasis in this preclinical oral cancer model. Using an optimal cutoff value of $S/B_{mean} \geq 1.35$ provided 75% SEN, 79% SPC, 77% ACC, and 71% NPV for pN+ staged nodes. Nearly all false positive nodes were from anatomical level 1 (86%) and completely overlapped with the false positive nodes from ^{64}Cu-PS PET. Nodes falsely labelled negative from FL imaging came evenly from both anatomical levels 1 (45%) and 2 (55%) and included the nodes mislabelled negative from ^{64}Cu-PS PET.

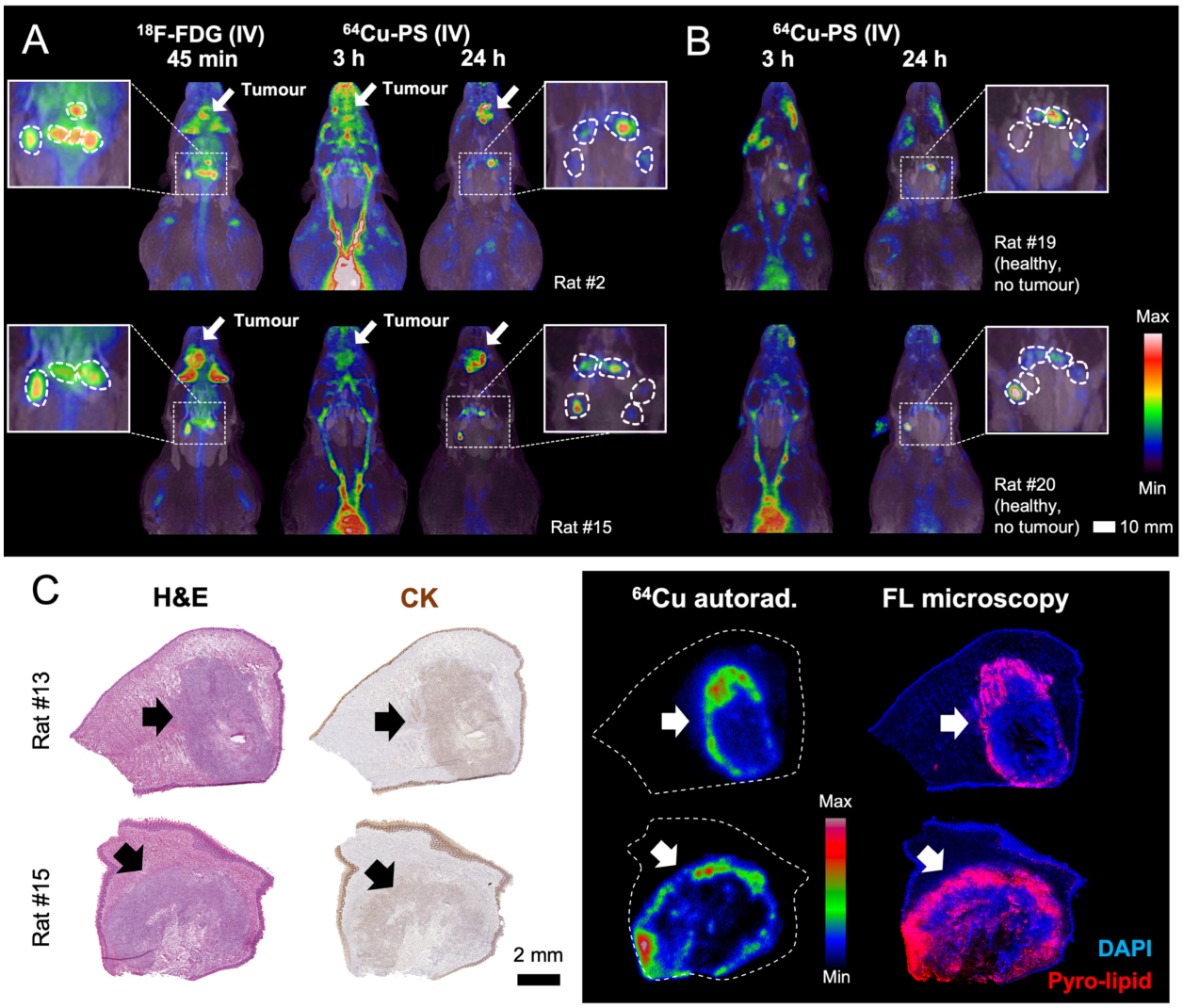

Figure 3. Uptake of ^{64}Cu-labelled PS in tongue tumours. (A) Representative MIPs of ^{18}F-FDG PET/MR images 45 min post-IV injection (46 MBq ^{18}F/kg), and ^{64}Cu-PS PET/MR images from 3 h and 24 h post-IV injection (250–500 MBq ^{64}Cu/kg, 0.5–1.0 mg/kg pyro-lipid) in tumour-bearing rats. Magnified view of outlined neck nodes in insets. Arrows denote tumour. ^{64}Cu PET signal intensity arbitrarily scaled to the 3 h timepoint. (B) Representative MIPs of ^{64}Cu-PS PET/MR images from healthy rats (i.e., without tongue tumours). (C) Representative histopathology of rat tongues with SCC tumours illustrating correspondence between CK$^+$ stained tumour cells, ^{64}Cu autoradiography signal, and pyro-lipid FL microscopy. Arrows denote tumour.

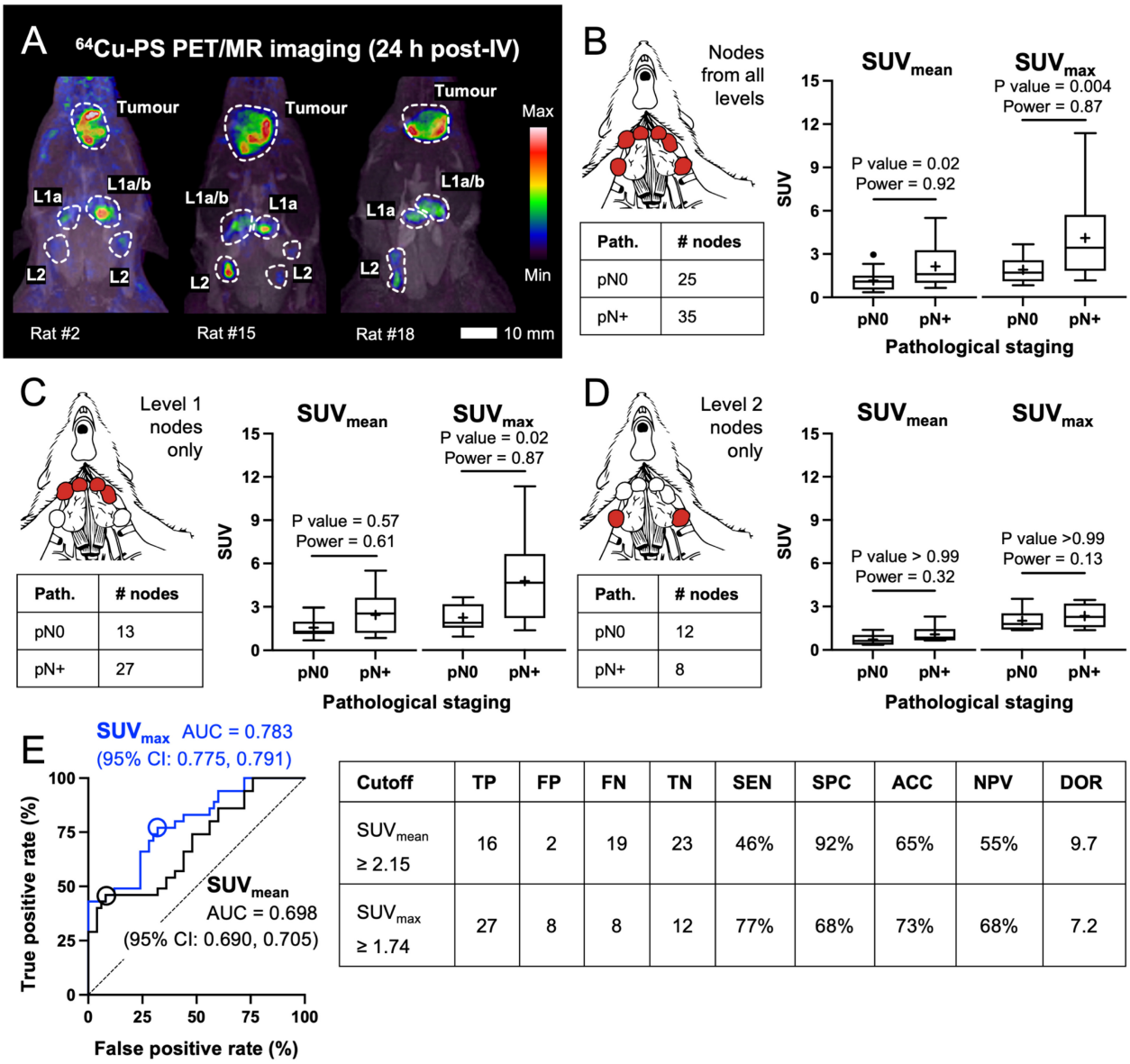

Cutoff	TP	FP	FN	TN	SEN	SPC	ACC	NPV	DOR
SUV_{mean} ≥ 2.15	16	2	19	23	46%	92%	65%	55%	9.7
SUV_{max} ≥ 1.74	27	8	8	12	77%	68%	73%	68%	7.2

Figure 4. PET imaging of ^{64}Cu-labelled PS uptake in neck lymph nodes of tongue tumour models. (A) Representative MIPs of ^{64}Cu-PS PET/MR images from 24 h post-IV injection (250–500 MBq ^{64}Cu/kg, 0.5–1.0 mg/kg pyro-lipid). ^{64}Cu-PS uptake in pN0 *vs* pN+ staged nodes from (B) all anatomical levels, (C) level 1 only, and (D) level 2 only. Tukey box-and-whisker plots with "+" at mean. SUVs unitless. Statistics compare pN0 *vs* pN+ staged nodes using multiple comparisons t tests with Tukey correction. Power analysis is a post hoc test of two independent means. (E) ROC curves and diagnostic performance of tests predicting pN+ staged nodes using 24 h PET imaging SUV. ROC AUCs and 95% CIs listed in brackets.

Discussion

The therapeutic benefits from elective neck dissections in early-stage oral cancer patients with cN0 necks are well evidenced [12,34], yet come at the expense of several treatment-related functional and cosmetic morbidities and impacted quality of life [35,36]. The motivation for these procedures is the estimated 10~30% of cN0 patients [12,13] whose undetected nodal disease creates significant risks for neck recurrences [37] requiring salvage treatments. Clinically occult neck metastases are typically microscopic, making their sensitive detection by preoperative imaging modalities difficult [18]. This unmet clinical need has motivated the development of novel contrast agents like ^{64}Cu-PS nanotheranostics to better detect occult neck metastases and potentially obviate the need for routine elective neck treatments altogether.

For this study, a T cell deficient athymic nude rat [38] was used to establish the oral cancer model with neck metastases (Fig. 1). Histological comparisons of cervical lymph nodes from athymic nude and immune competent rats have found microscopic differences in B cell zones like germinal centres (e.g., smaller and scarcer in nude rats), whereas T cell zones like the paracortex were still distinguishable, albeit laden with macrophages [39]. Several preclinical head

and neck cancer models have been described in immune competent rodents [40,41], but these typically lack reproducible development of cervical node metastases [42,43]. In immune deficient animals, higher incidences of neck disease are obtained [42], possibly from reduced tumour-immune cell interactions combating the seeding of lymphatic metastases. The role of T cell interactions on nanoparticle trafficking to metastatic lymph nodes is underexplored [44,45] with literature pointing to dominant interactions of smaller, neutrally charged particles like ^{64}Cu-PS with resident CD11b$^+$ macrophages and follicular B220$^+$ B cells, and only minor interactions with CD8$^+$ T cells [46–50].

In oral cancers, known changes to CD20$^+$ B cell and CD8$^+$ T cell localisation in metastatic cervical lymph nodes [51] may enhance interactions with nanoparticles in a way that is favourable for their selective retention in metastatic nodes. Unravelling the roles of specific lymphocyte populations on the differential uptake of ^{64}Cu-PS in benign and metastatic nodes (see Figs. 4, 5) was beyond this study's scope and warrants further investigation in immune competent metastasis models (e.g., rabbit VX-2 oral tumours [23,24]). Notably, such detailed cellular characterisations were not necessary for the successful clinical translation of fluorophore-labelled antibodies [52,53] and pH sensitive fluorescent micelles [54,55] for intraoperative FL imaging of oral SCC disease.

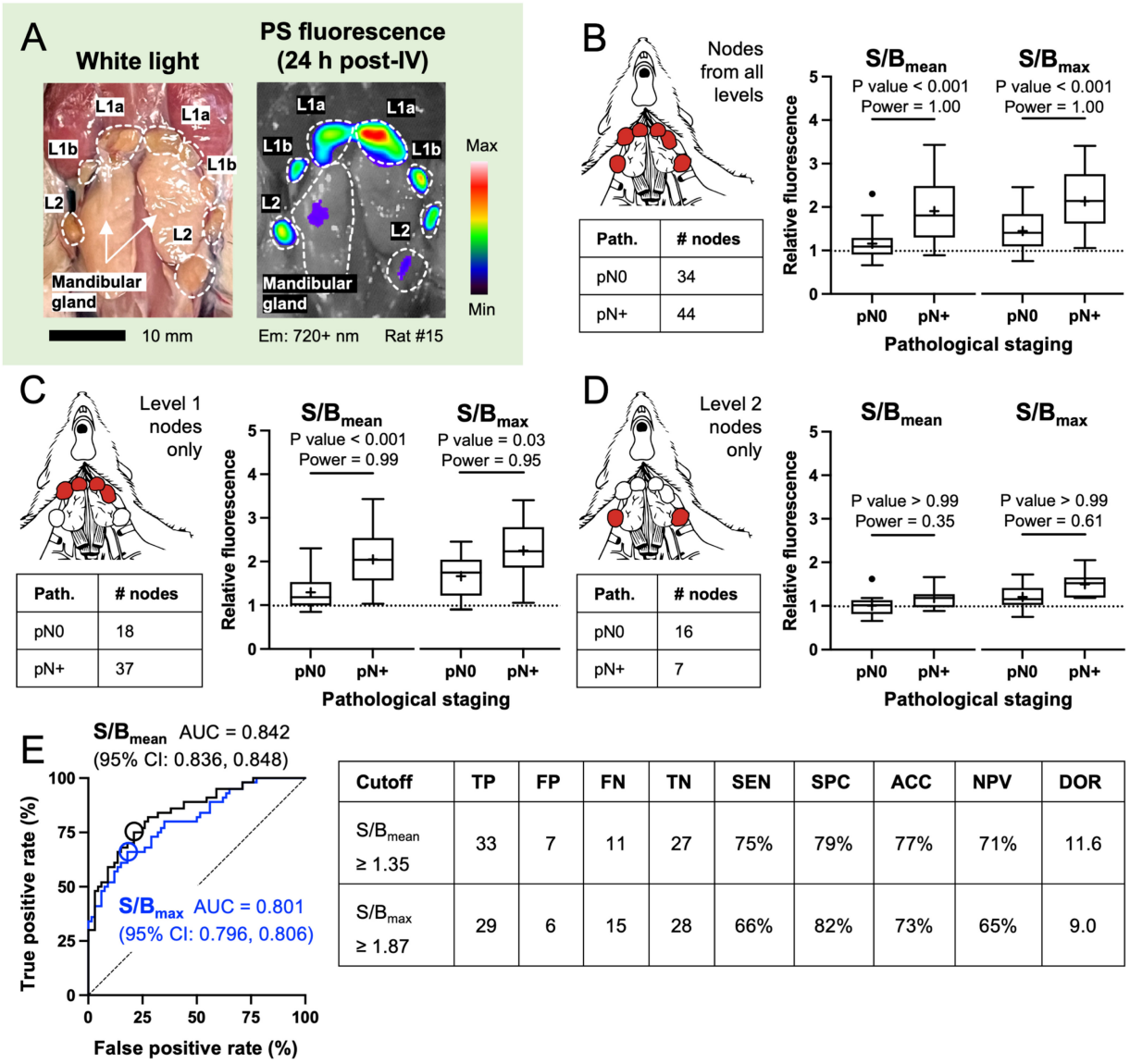

Cutoff	TP	FP	FN	TN	SEN	SPC	ACC	NPV	DOR
S/B_{mean} ≥ 1.35	33	7	11	27	75%	79%	77%	71%	11.6
S/B_{max} ≥ 1.87	29	6	15	28	66%	82%	73%	65%	9.0

Figure 5. *In situ* FL imaging of ^{64}Cu-labelled PS fluorescence in neck lymph nodes of tongue tumour models. (A) Representative white light and PS fluorescence images of neck nodes 24 h post-IV injection (0.5–1.0 mg/kg pyro-lipid). Relative PS fluorescence in pN0 *vs* pN+ staged nodes from (B) all anatomical levels, (C) level 1 only, and (D) level 2 only. Tukey box-and-whisker plots with "+" at mean. S/B ratios unitless. Statistics compare pN0 *vs* pN+ staged nodes using multiple comparisons t tests with Tukey correction. Power analysis is a post hoc test of two independent means. (E) ROC curves and diagnostic performance of tests predicting pN+ staged nodes using FL imaging S/B. ROC AUCs and 95% CIs listed in brackets.

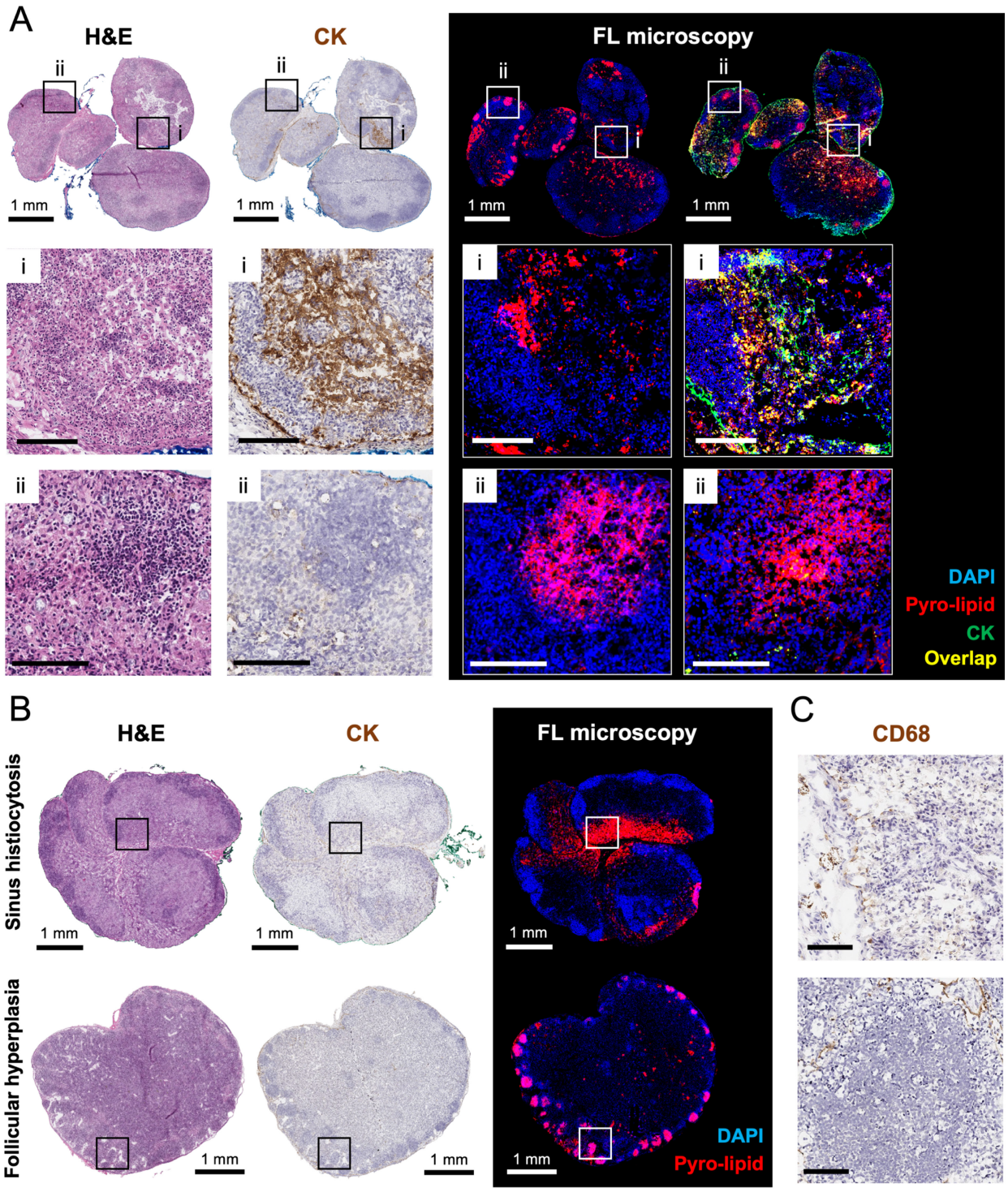

Figure 6. Histological microdistribution of ^{64}Cu-PS in neck lymph nodes of tongue tumour models. (A) Colocalisation of pyro-lipid FL signal with CK$^+$ stained SCC tumour cells in a pN+ staged "true positive" lymph node from ^{64}Cu-PS PET and FL imaging. Magnified views of pyro-lipid FL signal overlapping **with** (i) **CK$^+$ tumour cells** in the subcapsular sinus and (ii) in tumour-free nodal structures such as B cell rich follicles. (B) Examples of pN0-staged "false positive" lymph nodes from ^{64}Cu-PS PET and FL imaging illustrating nonspecific particle uptake in inflamed subcapsular sinuses (sinus histiocytosis) and follicles (follicular hyperplasia) with (C) CD68$^+$ staining for lymph node-resident dendritic cells and macrophages. Scale bar for all histology insets 100 µm.

The clinical standard of care using elective neck dissections for early-stage cN0 disease is being challenged by less invasive, less morbid sentinel node biopsy [56,57]; a technique measuring IT injected nanocolloidal radiotracer uptake in the first echelon cervical lymph node(s) with lymphoscintigraphy [58]. In Fig. 2 we demonstrate that IT injection of ^{64}Cu-PS similarly maps sentinel and other cervical nodes by PET imaging for up to 72 h. Uptake in pN+ staged nodes was higher on average than in pN0 nodes,

likely reflecting greater lymphatic flow from the tongue tumour [59] and lower retention of particles in benign nodes [60]. However, ^{64}Cu-PS PET signal differences between pN0 *vs* pN+ staged nodes were not significant enough to be diagnostic outright (Table S3), as is also the case with existing sentinel node radiotracers. A potential advantage of ^{64}Cu-PS is their inherent multimodality imaging, combining high resolution preoperative PET and intraoperative FL imaging. Several of the pitfalls with the sentinel lymph node biopsy in oral cancers—obstructed or redirected lymphatic flow [61], skip nodal metastases [62], etc.—will similarly affect the use of IT-injected ^{64}Cu-PS and motivate exploring IV administration.

Following systemic injection, ^{64}Cu-PS passively accumulated in the tongue tumour and drained to the cervical lymph nodes, yielding high contrast PET images of the tongue and neck by 24 h post-IV injection comparable to ^{18}F-FDG PET (Fig. 3A). Contrast from FL signal in lymph nodes *vs* background was also exceptionally high (Fig. 5A). ^{64}Cu-PS signal was measurably greater on average in pN+ *vs* pN0 staged lymph nodes by both PET (Fig. 4B-D) and *in situ* FL (Fig. 5B-D). The ROC AUC for ^{64}Cu-PS PET SUV_{max} was 0.783 (Fig. 4E) which was significantly greater than the 0.575 AUC for ^{18}F-FDG SUV_{mean} (Fig. S3). The highest ROC AUC obtained experimentally was 0.842 from ^{64}Cu-PS FL S/B_{mean} (Fig. 5E) which compares favourably to other clinically tested imaging agents for oral SCC disease [63,64]. The diagnostic performance of FL imaging S/B ratio superseded those with PET, confirming that *in situ* ^{64}Cu-PS FL imaging can serve as a standalone intraoperative modality.

An influential paper by Weiss *et al.* [65] on the management of oral cancer patients with cN0 staged necks established that if the probability of cervical lymph node metastasis exceeds 20%, then treatment of the neck by surgery or radiation is warranted. Thus, a diagnostic test must achieve NPV > 80% (i.e., probability that a node is pN0 after a "negative" imaging result) to waive elective neck treatments. Using the Youden index no imaging modality studied here exceeded 80% NPV (Table S10). With an algorithm optimising cutoff values for NPV ≥ 80%, only ^{64}Cu-PS imaging achieved this threshold: FL S/B_{mean} ratio ≥ 1.02 provided an 88% NPV with the trade-off of a 68% positive post-test probability from significant overstaging (i.e., type I error). Interestingly, across both imaging modalities lymph nodes from level 1 were consistently responsible for most "false positives" while missed "false negatives" originated primarily from level 2, a trend not seen with other agents like ^{18}F-FDG [16] and fluorophore-labelled antibodies [63,66].

Diagnostic imaging of head and neck cancers often include comparisons of lymph nodes by neck level and/or by neck side (e.g., ipsilateral *vs* contralateral, depending on primary tumour location) to improve accuracy for regional metastasis detection. In this study ^{64}Cu-PS signal differences between pN0 and pN+ nodes were analysed either pooled altogether (as in Figs. 4B, 5B) or separately by anatomical neck level (Figs. 4C-D, 5C-D). Neck level analyses were complicated by small sample sizes that underpowered statistical comparisons, particularly for level 2 nodes where the metastatic yield was only 11% (or 12/114 nodes, see Fig. 1C). At least 7 additional tumour-bearing rats would have been needed to sufficiently power this comparison, which given the modest differences between pN0 *vs* pN+ nodes at level 2 in ^{64}Cu-PS uptake (Fig. 4D) and relative FL (Fig. 5D) did not seem worthwhile.

The biological mechanisms by which nontargeted ^{64}Cu-PS preferentially accumulate in micrometastatic lymph nodes remain incompletely understood. Despite nonspecific uptake of IV injected ^{64}Cu-PS in the cervical neck nodes of healthy rats without tumours (Fig. 3B), the uptake (Fig. S4) and relative FL (Fig. S5) in benign and malignant nodes of tumour-bearing rats was greater on average. This observation suggests that increased lymphatic tumour drainage [59], enabling greater free particle flow through ~100 μm wide lymph vessels, was the dominant delivery pathway for ^{64}Cu-PS to the neck nodes. Vascular related mechanisms of accumulation like the enhanced permeability and retention (EPR) effect have been previously shown to occur only at more advanced stages of lymphatic disease, once metastatic deposits have evolved their own blood supply [60,67]; thus, EPR effect was not likely to have been a leading pathway for particle uptake in lymph node micrometastases.

In Fig. 6A is histological evidence for the colocalisation of the fluorescent pyro-lipid building blocks with CK^+ tumour cells in the subcapsular sinus, as well as evidence for nonspecific retention of particles in other benign structures of metastatic nodes such as lymphoid follicles. For nanoparticles with similar physicochemical properties to ^{64}Cu-PS (i.e., ~80 nm diameter, neutral PEGylated surface), literature describes variable uptake in $B220^+$ B cells microscopically located in the lymph node cortex [48,49] and in lymph node resident $CD68^+$ dendritic cells and macrophages located in the subcapsular and medullar sinuses [46–48,50]. The follicular uptake pattern of ^{64}Cu-PS in Fig. 6A was consistent across both pN0 and pN+ staged nodes, an unexpected observation when compared to other nanoparticle uptake studies in benign or malignant lymph nodes

[47,49,50,60]. This uptake pattern may reflect underlying biological differences in the lymph nodes of immune compromised rodents [39], increased translocation of macrophages to B cell rich follicles after ^{64}Cu-PS phagocytosis (i.e., for antigen presentation) [48,49], or even unintentional reprogramming of lymph node resident macrophages to pro-inflammatory M1 phenotypes from the low-level radioactivity of ^{64}Cu [68], all hypotheses warranting further investigation.

Reactive and inflamed lymph nodes (lymphadenitis) frequently confound diagnostic tests for lymph node metastases in head and neck cancer, leading to "false positive" findings on ^{18}F-FDG PET [69,70], with antibody-based optical imaging [63,66], and other nanoparticle-based theranostic imaging strategies [71,72]. Two examples of pN0-staged "false positive" nodes from both ^{64}Cu-PS PET and FL imaging are illustrated in Fig. 6B: significant particle uptake was observed in tumour-free lymph node structures with microscopic evidence of immunological reaction [73] and staining for CD68$^+$ macrophages and dendritic cells (see Fig. 6C). Nonspecific ^{64}Cu-PS uptake and retention in inflamed nodes may have prognostic relevance for patients, highlighting potential pre-metastatic niches in the neck for tumour cell colonisation [74] and sites of regional recurrences. Strategies for enabling clearer interpretation of benign, reactive, and metastatic lymph nodes, including serial imaging protocols [75,76] and dual-tracer injection approaches [77], have shown promise for other agents and may warrant further study with ^{64}Cu-PS.

Facing the future clinical translation of PS nanotheranostics, our group has completed extensive studies of PS pharmacology and toxicology in rodents and beagle dogs [27]. PS pharmacokinetics was dose proportional over a wide dose range, and single IV doses up to 32.6 mg/kg were safe in rats (compared to 0.5–1.0 mg/kg doses used here). A Good Manufacturing Practices-qualified radio pharmaceutical kit for labelling PS with 850 MBq [^{64}Cu]$CuCl_2$ was developed [27], and is producing patient doses for a first-in-human PET imaging study in metastatic cancer patients (NCT06977126). A 200 MBq ^{64}Cu-PS dose was selected for patients based on prior clinical data with radiolabelled liposomes [78] and is predicted to give an effective radiation dose in patients between 7.6–9.4 mSv [27], or about half the radiation dose from a routine ^{18}F-FDG oncology scan (14.1 mSv average effective dose [79]). Future study phases will expand the eligibility for ^{64}Cu-PS to include oral cancer patients with known or suspected regional lymph node involvement and scheduled for neck dissection.

Conclusions

In summary we have demonstrated the diagnostic performance of ^{64}Cu-PS nanotheranostics for identifying metastatic cervical lymph nodes in rats bearing tongue tumours. These nontargeted agents permitted more accurate detection of microscopic neck disease than conventional imaging techniques such as MR imaging (for cervical lymph node morphology) and molecular imaging using metabolic ^{18}F-FDG PET. The unique multifunctionality of ^{64}Cu-PS combining PET and near infrared FL imaging enables both pre- and intraoperative guidance for planning and performing neck dissections in oral cancer patients with greater precision. Altogether these results motivate the continued development of porphyrin-lipid nanotheranostics for clinical studies in oral cancer patients with clinically occult neck disease.

Abbreviations

ACC: accuracy; A_s: specific activity; AUC: area under the curve; CK: cytokeratin staining; C_{max}: maximum tissue concentration; cN0: clinical lymph node-negative status; ^{64}Cu-PS: ^{64}Cu-Porphysomes, PEGylated [^{64}Cu]pyro-lipid nanoparticles; CT: computed tomographic imaging; DAPI: 4′,6-diamidino-2-phenylindole; DOR: diagnostic odds ratio; EPR: enhanced permeability and retention; ^{18}F-FDG: [^{18}F]Fluorodeoxyglucose; FL: fluorescence imaging; FN: false negative; FP: false positive; H&E: haematoxylin and eosin staining; %I.D.: percent injected dose; IT: intratumoural; IV: intravenous; LN: lymph node; MIP: mean intensity projection; MOC2: mouse oral squamous cell carcinoma; MR: magnetic resonance imaging; N/A: not applicable; NPV: negative predictive value; PET: positron emission tomographic imaging; pN0: pathological lymph node-negative status; pN+: pathological lymph node-positive status; PPV: positive predictive value; PS: Porphysomes, PEGylated pyro-lipid nanoparticles; ROC: receiver operating characteristic curve; ROI: region of interest; S/B: signal-to-background ratio; SCC: squamous cell carcinoma; SEN: sensitivity; SPC: specificity; SUV: standardised uptake value; TN: true negative; TP: true positive; VOI: volume of interest.

Supplementary Material

Supplementary figures and tables.
https://www.thno.org/v16p7108s1.pdf

Acknowledgments

We thank Feryal Sarraf and Napoleon Law of the STTARR Innovation Centre for assistance with

histology; Deborah Scollard, Teesha Komal, Luke Yongkyu Kwon, Alberto Cevallos and Rita Chen of the STTARR Innovation Centre for assistance with radioactive studies involving animals; Andrea Archila, Maria Bisa, Nancy Dean, Jenn Latanski, Kathleen Ma and Audrey Pang of UHN ARC for assistance with animal experiments.

This work was supported by the Terry Fox Research Institute New Frontiers Program Project Grant #1075 and #1137, the Canadian Cancer Society Challenge Grant #707426, the Canada Research Chairs Program (950-232468), the US Department of Defense Award #W81XWH-12-1-0442, and the Princess Margaret Cancer Foundation.

Data availability

The data generated in this study are available upon request.

Contributions

Michael Valic: conceptualization, methodology, validation, formal analysis, investigation, data curation, writing – original draft, writing – review & editing, visualization, funding acquisition. **Esmat Najjar:** conceptualization, methodology, investigation, resources, writing – original draft, writing – review & editing, visualization. **Mark Zheng:** software, validation, formal analysis, investigation, data curation, writing – original draft, visualization. **Jason Townson:** conceptualization, methodology, resources, writing – review & editing, project administration, funding acquisition. **Harley Chan:** methodology, investigation, resources. **Sharon Tzelnick:** investigation, data curation, resources. **Alessandra Ruaro:** investigation, data curation, resources. **Abdullah El-Sayes:** investigation, resources. **Michael Halim:** investigation, resources. **Pamela Schimmer:** investigation, resources. **Chris Zhang:** investigation, resources. **Tina Ye:** investigation, resources. **Wenlei Jiang:** methodology, investigation, resources. **Juan Chen:** investigation, resources, writing – review & editing, project administration, funding acquisition. **Jonathan Irish:** conceptualization, writing – review & editing, supervision, funding acquisition. **Gang Zheng:** conceptualization, writing – review & editing, supervision, project administration, funding acquisition.

Disclaimers

Parts of this work has been previously presented as an abstract (ID #LB225) at the 2025 World Molecular Imaging Congress.

Ethics approval for animal studies

Animal studies were conducted at the University Health Network in accordance with protocol #6207 approved by the Ontario Cancer Institute Animal Care Committee.

ORCIDs

Michael S. Valic (ORCID: 0000-0003-3488-023X).
Jonathan C. Irish (ORCID: 0000-0002-1631-2717).
Gang Zheng (ORCID: 0000-0002-0705-7398).

Competing Interests

Michael Valic and Gang Zheng declare equity ownership in Nanogenix Inc. (Chicago, USA), a company commercializing Porphysomes for cancer imaging and phototherapy. No representative of Nanogenix other than those listed among the authors edited, reviewed, or otherwise influenced the reporting of results in this manuscript. The remaining authors declare no potential conflicts of interest.

References

1. Surveillance Research Program, National Cancer Institute. Oral Cavity and Pharynx Recent Trends in SEER Age-Adjusted Incidence Rates, 2000-2020. SEER Incidence Data, November 2022 Submission (1975-2020), SEER 22 registries; 2023.
2. Vandenbrouck C, Sancho-Garnier H, Chassagne D, Saravane D, Cachin Y, Micheau C. Elective versus therapeutic radical neck dissection in epidermoid carcinoma of the oral. Cavity results of a randomized clinical trial. Cancer. 1980; 46: 386–90.
3. Shah JP, Candela FC, Poddar AK. The patterns of cervical lymph node metastases from squamous carcinoma of the oral cavity. Cancer. 1990; 66: 109–13.
4. Woolgar JA. Detailed topography of cervical lymph-node metastases from oral squamous cell carcinoma. International Journal of Oral and Maxillofacial Surgery. 1997; 26: 3–9.
5. Woolgar JA. The topography of cervical lymph node metastases revisited: the histological findings in 526 sides of neck dissection from 439 previously untreated patients. International Journal of Oral and Maxillofacial Surgery. 2007; 36: 219–25.
6. Woolgar JA. Micrometastasis in oral/oropharyngeal squamous cell carcinoma: incidence, histopathological features and clinical implications. British Journal of Oral and Maxillofacial Surgery. 1999; 37: 181–6.
7. Olsen KD, Caruso M, Foote RL, et al. Primary Head and Neck Cancer: Histopathologic Predictors of Recurrence After Neck Dissection in Patients with Lymph Node Involvement. Archives of Otolaryngology - Head and Neck Surgery. 1994; 120: 1370–4.
8. Ho AS, Kim S, Tighiouart M, et al. Metastatic Lymph Node Burden and Survival in Oral Cavity Cancer. JCO. 2017; 35: 3601–9.
9. NCCN Clinical Practice Guidelines in Oncology: Head and Neck Cancers. 2025.
10. De Bondt RBJ, Nelemans PJ, Hofman PAM, et al. Detection of lymph node metastases in head and neck cancer: A meta-analysis comparing US, USgFNAC, CT and MR imaging. European Journal of Radiology. 2007; 64: 266–72.
11. Kyzas PA, Evangelou E, Denaxa-Kyza D, Ioannidis JPA. 18F-Fluorodeoxyglucose Positron Emission Tomography to Evaluate Cervical Node Metastases in Patients with Head and Neck Squamous Cell Carcinoma: A Meta-analysis. JNCI: Journal of the National Cancer Institute. 2008; 100: 712–20.
12. Massey C, Dharmarajan A, Bannuru RR, Rebeiz E. Management of N0 neck in early oral squamous cell carcinoma: A systematic review and meta-analysis. The Laryngoscope [Internet]. 2019 [cited 16 October 2024]; 129. Available at: https://onlinelibrary.wiley.com/doi/10.1002/lary.27627
13. Sharbel DD, Abkemeier M, Groves MW, Albergotti WG, Byrd JK, Reyes-Gelves C. Occult Metastasis in Laryngeal Squamous Cell Carcinoma: A Systematic Review and Meta-Analysis. Ann Otol Rhinol Laryngol. 2021; 130: 67–77.
14. Kim SY, Beer M, Tshering Vogel DW. Imaging in head and neck cancers: Update for non-radiologist. Oral Oncology. 2021; 120: 105434.
15. Liao L-J, Lo W-C, Hsu W-L, Wang C-T, Lai M-S. Detection of cervical lymph node metastasis in head and neck cancer patients with clinically N0 neck—a

meta-analysis comparing different imaging modalities. BMC Cancer. 2012; 12: 236.
16. Schöder H, Carlson DL, Kraus DH, et al. 18F-FDG PET/CT for Detecting Nodal Metastases in Patients with Oral Cancer Staged N0 by Clinical Examination and CT/MRI. J Nucl Med. 2006; 47: 755.
17. Stoeckli SJ, Haerle SK, Strobel K, Haile SR, Hany TF, Schuknecht B. Initial staging of the neck in head and neck squamous cell carcinoma: A comparison of CT, PET/CT, and ultrasound-guided fine-needle aspiration cytology. Head & Neck. 2012; 34: 469–76.
18. De Bree R, Takes RP, Castelijns JA, et al. Advances in diagnostic modalities to detect occult lymph node metastases in head and neck squamous cell carcinoma. Head & Neck. 2015; 37: 1829–39.
19. Krishnan G, Van Den Berg NS, Nishio N, et al. Fluorescent Molecular Imaging Can Improve Intraoperative Sentinel Margin Detection in Oral Squamous Cell Carcinoma. J Nucl Med. 2022; 63: 1162–8.
20. De Wit JG, Vonk J, Voskuil FJ, et al. EGFR-targeted fluorescence molecular imaging for intraoperative margin assessment in oral cancer patients: a phase II trial. Nat Commun. 2023; 14: 4952.
21. Vonk J, De Wit JG, Voskuil FJ, et al. Epidermal growth factor receptor targeted fluorescence molecular imaging for postoperative lymph node assessment in patients with oral cancer. J Nucl Med. 2021; jnumed.121.262530.
22. Krishnan G, Berg NSVD, Nishio N, et al. Metastatic and sentinel lymph node mapping using intravenously delivered Panitumumab-IRDye800CW. Theranostics. 2021; 11: 7188–98.
23. Muhanna N, MacDonald TD, Chan H, et al. Multimodal Nanoparticle for Primary Tumor Delineation and Lymphatic Metastasis Mapping in a Head-and-Neck Cancer Rabbit Model. Adv Healthcare Mater. 2015; 4: 2164–9.
24. Muhanna N, Cui L, Chan H, et al. Multimodal Image-Guided Surgical and Photodynamic Interventions in Head and Neck Cancer: From Primary Tumor to Metastatic Drainage. Clin Cancer Res. 2016; 22: 961–70.
25. Sahovaler A, Valic MS, Townson JL, et al. Nanoparticle-mediated Photodynamic Therapy as a Method to Ablate Oral Cavity Squamous Cell Carcinoma in Preclinical Models. Cancer Research Communications. 2024; 4: 796–810.
26. Liu TW, MacDonald TD, Shi J, Wilson BC, Zheng G. Intrinsically Copper-64-Labeled Organic Nanoparticles as Radiotracers. Angew Chem Int Ed. 2012; 51: 13128–31.
27. Valic MS, Fisher CJ, Zheng M, et al. Radiopharmaceutical kit to prepare Copper-64 labelled porphyrin-lipid nanoparticles for radiotracer imaging studies in cancer patients. Eur J Nucl Med Mol Imaging. 2025; 53: 663–86.
28. Lovell JF, Jin CS, Huynh E, et al. Porphysome nanovesicles generated by porphyrin bilayers for use as multimodal biophotonic contrast agents. Nature Mater. 2011; 10: 324–32.
29. Kono M, Saito S, Egloff AM, Allen CT, Uppaluri R. The mouse oral carcinoma (MOC) model: A 10-year retrospective on model development and head and neck cancer investigations. Oral Oncology. 2022; 132: 106012.
30. Hermanek P, Hutter RVP, Sobin LH, Wittekind C. Classification of isolated tumor cells and micrometastasis. Cancer. 1999; 86: 2668–73.
31. Devaney KO, Rinaldo A, Ferlito A. Micrometastases in cervical lymph nodes from patients with squamous carcinoma of the head and neck: should they be actively sought? Maybe. American Journal of Otolaryngology. 2007; 28: 271–4.
32. Sano D, Myers JN. Metastasis of squamous cell carcinoma of the oral tongue. Cancer Metastasis Rev. 2007; 26: 645–62.
33. Werner JA, Dünne AA, Myers JN. Functional anatomy of the lymphatic drainage system of the upper aerodigestive tract and its role in metastasis of squamous cell carcinoma. Head & Neck. 2003; 25: 322–32.
34. Kumar A, Ghai S, Mhaske S, Singh R. Elective Neck Dissection Versus Therapeutic Neck Dissection in Clinically Node-Negative Early Stage Oral Cancer: A Meta-analysis of Randomized Controlled Trials. J Maxillofac Oral Surg. 2022; 21: 340–9.
35. Van Wilgen CP, Dijkstra PU, Van Der Laan BFAM, Plukker JT, Roodenburg JLN. Morbidity of the neck after head and neck cancer therapy. Head & Neck. 2004; 26: 785–91.
36. Rogers SN, Ferlito A, Pellitteri PK, Shaha AR, Rinaldo A. Quality of life following neck dissections. Acta Oto-Laryngologica. 2004; 124: 231–6.
37. Rodrigo JP, Shah JP, Silver CE, et al. Management of the clinically negative neck in early-stage head and neck cancers after transoral resection. Head & Neck. 2011; 33: 1210–9.
38. Vos JG, Kreeftenberg JG, Kruijt BC, Kruizinga W, Steerenberg P. The athymic nude rat. Clinical Immunology and Immunopathology. 1980; 15: 229–37.
39. Fossum S, Smith ME, Bell EB, Ford WL. The Architecture of Rat Lymph Nodes: III. The Lymph Nodes and Lymph-borne Cells of the Congenitally Athymic Nude Rat (rnu). Scand J Immunol. 1980; 12: 421–32.
40. Hawkins BL, Heniford BW, Ackermann DM, Leonberger M, Martinez SA, Hendler FJ. 4NQO carcinogenesis: A mouse model of oral cavity squamous cell carcinoma. Head & Neck. 1994; 16: 424–32.
41. Tang X-H, Knudsen B, Bemis D, Tickoo S, Gudas LJ. Oral Cavity and Esophageal Carcinogenesis Modeled in Carcinogen-Treated Mice. Clinical Cancer Research. 2004; 10: 301–13.
42. Sano D, Myers JN. Xenograft models of head and neck cancers. Head Neck Oncol. 2009; 1: 32.
43. Supsavhad W, Dirksen WP, Martin CK, Rosol TJ. Animal models of head and neck squamous cell carcinoma. The Veterinary Journal. 2016; 210: 7–16.
44. Schudel A, Francis DM, Thomas SN. Material design for lymph node drug delivery. Nat Rev Mater. 2019; 4: 415–28.
45. Lan H-R, Zhang Y-N, Han Y-J, et al. Multifunctional nanocarriers for targeted drug delivery and diagnostic applications of lymph nodes metastasis: a review of recent trends and future perspectives. J Nanobiotechnol. 2023; 21: 247.
46. Oussoren C, Velinova M, Scherphof G, Van Der Want JJ, Van Rooijen N, Storm G. Lymphatic uptake and biodistribution of liposomes after subcutaneous injection IV. Fate of liposomes in regional lymph nodes. Biochimica et Biophysica Acta (BBA) - Biomembranes. 1998; 1370: 259–72.
47. Reddy ST, Rehor A, Schmoekel HG, Hubbell JA, Swartz MA. In vivo targeting of dendritic cells in lymph nodes with poly(propylene sulfide) nanoparticles. Journal of Controlled Release. 2006; 112: 26–34.
48. Manolova V, Flace A, Bauer M, Schwarz K, Saudan P, Bachmann MF. Nanoparticles target distinct dendritic cell populations according to their size. Eur J Immunol. 2008; 38: 1404–13.
49. Nakamura T, Kawai M, Sato Y, Maeki M, Tokeshi M, Harashima H. The Effect of Size and Charge of Lipid Nanoparticles Prepared by Microfluidic Mixing on Their Lymph Node Transitivity and Distribution. Mol Pharmaceutics. 2020; 17: 944–53.
50. Bennett ZT, Feng Q, Bishop JA, Huang G, Sumer BD, Gao J. Detection of Lymph Node Metastases by Ultra-pH-Sensitive Polymeric Nanoparticles. Theranostics. 2020; 10: 3340–50.
51. Pretscher D, Distel LV, Grabenbauer GG, Wittlinger M, Buettner M, Niedobitek G. Distribution of immune cells in head and neck cancer: CD8+ T-cells and CD20+B-cells in metastatic lymph nodes are associated with favourable outcome in patients with oro- and hypopharyngeal carcinoma. BMC Cancer. 2009; 9: 292.
52. Heath CH, Deep NL, Sweeny L, Zinn KR, Rosenthal EL. Use of Panitumumab-IRDye800 to Image Microscopic Head and Neck Cancer in an Orthotopic Surgical Model. Ann Surg Oncol. 2012; 19: 3879–87.
53. Day KE, Beck LN, Deep NL, Kovar J, Zinn KR, Rosenthal EL. Fluorescently labeled therapeutic antibodies for detection of microscopic melanoma. The Laryngoscope. 2013; 123: 2681–9.
54. Zhao T, Huang G, Li Y, et al. A transistor-like pH nanoprobe for tumour detection and image-guided surgery. Nat Biomed Eng. 2016; 1: 0006.
55. Huang G, Zhao T, Wang C, et al. PET imaging of occult tumours by temporal integration of tumour-acidosis signals from pH-sensitive 64Cu-labelled polymers. Nat Biomed Eng. 2019; 4: 314–24.
56. Garrel R, Poissonnet G, Moyà Plana A, et al. Equivalence Randomized Trial to Compare Treatment on the Basis of Sentinel Node Biopsy Versus Neck Node Dissection in Operable T1-T2N0 Oral and Oropharyngeal Cancer. JCO. 2020; 38: 4010–8.
57. Hasegawa Y, Tsukahara K, Yoshimoto S, et al. Neck Dissections Based on Sentinel Lymph Node Navigation Versus Elective Neck Dissections in Early Oral Cancers: A Randomized, Multicenter, and Noninferiority Trial. JCO. 2021; 39: 2025–36.
58. The European Association of Nuclear Medicine (EANM) Oncology Committee and European Sentinel Node Biopsy Trial (SENT) Committee, Alkureishi LWT, Burak Z, et al. Joint Practice Guidelines for Radionuclide Lymphoscintigraphy for Sentinel Node Localization in Oral/Oropharyngeal Squamous Cell Carcinoma. Ann Surg Oncol. 2009; 16: 3190–210.
59. Hoshida T, Isaka N, Hagendoorn J, et al. Imaging Steps of Lymphatic Metastasis Reveals That Vascular Endothelial Growth Factor-C Increases Metastasis by Increasing Delivery of Cancer Cells to Lymph Nodes: Therapeutic Implications. Cancer Research. 2006; 66: 8065–75.
60. Cabral H, Makino J, Matsumoto Y, et al. Systemic Targeting of Lymph Node Metastasis through the Blood Vascular System by Using Size-Controlled Nanocarriers. ACS Nano. 2015; 9: 4957–67.
61. Civantos FJ, Gomez C, Duque C, et al. Sentinel node biopsy in oral cavity cancer: Correlation with PET scan and immunohistochemistry. Head & Neck. 2003; 25: 1–9.
62. Civantos FJ, Stoeckli SJ, Takes RP, et al. What is the role of sentinel lymph node biopsy in the management of oral cancer in 2010? Eur Arch Otorhinolaryngol. 2010; 267: 839–44.
63. Nishio N, Van Den Berg NS, Van Keulen S, et al. Optical molecular imaging can differentiate metastatic from benign lymph nodes in head and neck cancer. Nat Commun. 2019; 10: 5044.
64. Meeks N, James S, Krishnan G, et al. Background Tissue with Native Target Expression Can Determine Presence of Nodal Metastasis in Head and Neck Squamous Cell Carcinoma Patients Infused with Targeted Fluorescent Tracers. Mol Imaging Biol. 2025; 27: 333–40.
65. Weiss MH, Harrison LB, Isaacs RS. Use of Decision Analysis in Planning a Management Strategy for the Stage NO Neck. Archives of Otolaryngology - Head and Neck Surgery. 1994; 120: 699–702.
66. Rosenthal EL, Moore LS, Tipirneni K, et al. Sensitivity and Specificity of Cetuximab-IRDye800CW to Identify Regional Metastatic Disease in Head and Neck Cancer. Clinical Cancer Research. 2017; 23: 4744–52.
67. Mikada M, Sukhbaatar A, Miura Y, et al. Evaluation of the enhanced permeability and retention effect in the early stages of lymph node metastasis. Cancer Science. 2017; 108: 846–52.
68. Klug F, Prakash H, Huber PE, et al. Low-Dose Irradiation Programs Macrophage Differentiation to an iNOS+/M1 Phenotype that Orchestrates Effective T Cell Immunotherapy. Cancer Cell. 2013; 24: 589–602.

69. Nakagawa T, Yamada M, Suzuki Y. 18 F-FDG Uptake in Reactive Neck Lymph Nodes of Oral Cancer: Relationship to Lymphoid Follicles. J Nucl Med. 2008; 49: 1053–9.
70. Troost EGC, Bussink J, Oyen WJG, Kaanders JHAM. 18 F-FDG and18 F-FLT Do Not Discriminate Between Reactive and Metastatic Lymph Nodes in Oral Cancer. J Nucl Med. 2009; 50: 490–1.
71. Mack MG, Balzer JO, Straub R, Eichler K, Vogl TJ. Superparamagnetic Iron Oxide–enhanced MR Imaging of Head and Neck Lymph Nodes. Radiology. 2002; 222: 239–44.
72. Sigal R, Vogl T, Casselman J, et al. Lymph node metastases from head and neck squamous cell carcinoma: MR imaging with ultrasmall superparamagnetic iron oxide particles (Sinerem MR) – results of a phase-III multicenter clinical trial. Eur Radiol. 2002; 12: 1104–13.
73. Valk VD, Meijer CJLM. The Histology of Reactive Lymph Nodes: The American Journal of Surgical Pathology. 1987; 11: 866–82.
74. Pereira ER, Jones D, Jung K, Padera TP. The lymph node microenvironment and its role in the progression of metastatic cancer. Seminars in Cell & Developmental Biology. 2015; 38: 98–105.
75. Hustinx R, Smith RJ, Benard F, et al. Dual time point fluorine-18 fluorodeoxyglucose positron emission tomography: a potential method to differentiate malignancy from inflammation and normal tissue in the head and neck. Eur J Nucl Med. 1999; 26: 1345.
76. Soffers F, Helsen N, Van Den Wyngaert T, et al. Dual time point imaging in locally advanced head and neck cancer to assess residual nodal disease after chemoradiotherapy. EJNMMI Res. 2022; 12: 34.
77. Tichauer KM, Samkoe KS, Gunn JR, et al. Microscopic lymph node tumor burden quantified by macroscopic dual-tracer molecular imaging. Nat Med. 2014; 20: 1348–53.
78. Lee H, Shields AF, Siegel BA, et al. 64 Cu-MM-302 Positron Emission Tomography Quantifies Variability of Enhanced Permeability and Retention of Nanoparticles in Relation to Treatment Response in Patients with Metastatic Breast Cancer. Clin Cancer Res. 2017; 23: 4190–202.
79. Mettler FA, Huda W, Yoshizumi TT, Mahesh M. Effective Doses in Radiology and Diagnostic Nuclear Medicine: A Catalog. Radiology. 2008; 248: 254–63.